Nonlocal signatures of the chiral magnetic effect in the Dirac semimetal $Bi_{0.97}Sb_{0.03}$

Jorrit C. de Boer,[1,*] Daan H. Wielens,[1,*] Joris A. Voerman,[1] Bob de Ronde,[1] Yingkai Huang,[2] Mark S. Golden,[2] Chuan Li,[1] and Alexander Brinkman[1]

[1]*MESA$^+$ Institute for Nanotechnology, University of Twente, The Netherlands*

[2]*Van der Waals - Zeeman Institute, IoP, University of Amsterdam, The Netherlands*

(Received 19 November 2018; revised manuscript received 9 January 2019; published 13 February 2019)

The field of topological materials science has recently been focusing on three-dimensional Dirac semimetals, which exhibit robust Dirac phases in the bulk. However, the absence of characteristic surface states in accidental Dirac semimetals (DSMs) makes it difficult to experimentally verify claims about the topological nature using commonly used surface-sensitive techniques. The chiral magnetic effect (CME), which originates from the Weyl nodes, causes an $\mathbf{E}\cdot\mathbf{B}$-dependent chiral charge polarization, which manifests itself as negative magnetoresistance. We exploit the extended lifetime of the chirally polarized charge and study the CME through both local and nonlocal measurements in Hall bar structures fabricated from single crystalline flakes of the DSM $Bi_{0.97}Sb_{0.03}$. From the nonlocal measurement results we find a chiral charge relaxation time, which is over one order of magnitude larger than the Drude transport lifetime, underlining the topological nature of $Bi_{0.97}Sb_{0.03}$.

DOI: 10.1103/PhysRevB.99.085124

I. INTRODUCTION

The electronic structure of bismuth-antimony alloys has been thoroughly studied in the 1960s and 70s and later regained attention when $Bi_{1-x}Sb_x$ was one of the first topological materials to be discovered [1]. It was proposed that at the topological transition point, which is at $x \sim 0.03$, an accidental band touching in the bulk of $Bi_{1-x}Sb_x$ makes this material a Dirac semimetal (DSM) [2–4]. A popular method to measure the topological nature of DSMs is through the detection of the chiral magnetic effect (CME) in electronic transport measurements. However, these signals are often obscured by the presence of parallel, nontopological conduction channels and are, more importantly, difficult to distinguish from other effects that may cause negative magnetoresistance, such as current jetting [5]. Parameswaran *et al.* [6] proposed to measure the CME nonlocally, using the extended lifetime of chirally polarized charge. For the Dirac semimetal Cd_3As_2, where two sets of Dirac cones with opposite chirality are separated in momentum space and protected by inversion symmetry, this measurement technique has been successfully used to measure the CME [7]. In this work, we present evidence for the presence of the chiral magnetic effect in the accidental Dirac semimetal $Bi_{0.97}Sb_{0.03}$, based on local and nonlocal magnetotransport results on crystalline, exfoliated flakes.

In a general Dirac semimetal, two Weyl cones of opposite chirality (often labeled as isospin degree of freedom [6]) are superposed in momentum space as depicted in Fig. 1(a). Their chiralities are defined through an integral of the Berry connection, $A_{\mathbf{k}\pm} = i\langle\psi_\pm|\nabla_{\mathbf{k}}\psi_\pm\rangle$, over the Fermi surface (FS):

$$\chi_\pm = \frac{1}{2\pi}\oint_{FS}(\nabla_{\mathbf{k}}\times A_{\mathbf{k}\pm})\cdot dS_{\mathbf{k}}, \tag{1}$$

where $\boldsymbol{k}$ is the wave vector. Using a basic representation of the Weyl nodes, $\psi_\pm = [e^{-i\theta}\sin(\phi/2), -\cos(\phi/2)]^T$ (where θ is the in-plane angle in momentum space, with $\theta = 0$ along the k_x axis, and ϕ is the polar angle with respect to k_z), one finds $\chi_\pm = \pm 1$. These nodes with opposite chiralities always come in pairs and, when the degeneracy of the Weyl cones is lifted, they are connected in momentum space by a surface state known as a Fermi arc. In mirror symmetry-protected Dirac systems, such as Cd_3As_2, different pairs of Weyl nodes can also be connected by Fermi arcs, which has been experimentally observed [8]. $Bi_{0.97}Sb_{0.03}$ contains accidental Dirac points at the three L points [2]. The crossings at these Dirac points are not protected by any symmetry, and should not be connected by Fermi arcs. However, upon breaking time-reversal symmetry with an external magnetic field, the Dirac cones split into two Weyl cones of opposite chirality, in which case $Bi_{0.97}Sb_{0.03}$ behaves very similar to Cd_3As_2. A more in-depth discussion on the topological properties of $Bi_{0.97}Sb_{0.03}$ compared to those of Cd_3As_2 can be found in Sec. A of the Supplemental Material [9].

The different chiral nodes correspond to a source and drain of Berry curvature ($\Omega_{\mathbf{k}\pm} = \nabla_{\mathbf{k}}\times A_{\mathbf{k}\pm}$), which in turn behaves as a magnetic field in momentum space. Taking this momentum space analog of the magnetic field into account in the equations of motion, one ends up with an expression for chiral charge pumping $\partial\rho_\pm/\partial t$ in external parallel electric and magnetic fields [10,11]:

$$\frac{\partial\rho_\pm}{\partial t} = f(\Omega_{\mathbf{k}})\frac{e^3}{4\pi^2\hbar^2}\mathbf{E}\cdot\mathbf{B}, \tag{2}$$

where $\boldsymbol{E}$ and $\boldsymbol{B}$ are the electric and magnetic fields respectively, and $f(\Omega_{\mathbf{k}})$ represents the chirality dependence. The result from this semiclassical argument can also been obtained in the quantum limit [12]. This chiral charge pumping creates a difference in chemical potential in the two Weyl cones, causing a net imbalance in chirality, which eventually relaxes by means of impurity scattering. However, the orthogonality of the two degenerate Weyl cones with different isospin and the large momentum difference between different valleys

[*]These two authors contributed equally to this work.

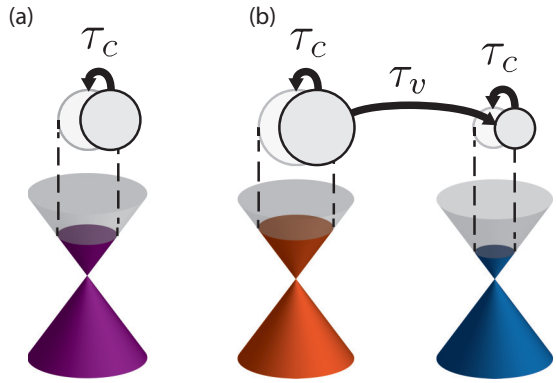

FIG. 1. Dirac semimetals and the chiral magnetic effect. (a) Two superposed Weyl cones in a Dirac semimetal. In an external electric field, the electrons on a shifted Fermi surface relax to their equilibrium state with characteristic time τ_c. (b) In parallel external electric and magnetic fields, the two Weyl cones are separated in momentum space and exhibit different chemical potentials. Intercone relaxation of chirally polarized electrons occurs with characteristic time τ_{CME}.

suppress these relaxation processes. As a consequence, chiral charge has an increased lifetime compared to the Drude transport lifetime, which is shortened by many low-energy scattering events. Through the continuity equations, this chiral charge imbalance contributes to the longitudinal conductivity and can be observed in magnetotransport measurements [2,13].

In Cd_3As_2, there are two scattering events that relax the chiral charge polarization: scattering between degenerate cones of different isospin, and intervalley scattering. Of these two, intervalley scattering should be expected to be the dominant factor as the momentum difference between the valleys is relatively small [7]. In $Bi_{0.97}Sb_{0.03}$, where the Dirac points reside at the three L points, intervalley scattering requires a momentum transfer of the order $2\pi/a$, with a being the lattice constant. Because of this required large momentum transfer, we argue that isospin-flip scattering through multiple scattering events is the likely dominant chiral relaxation process in $Bi_{0.97}Sb_{0.03}$.

II. METHODS AND CHARACTERIZATION

To characterize the $Bi_{0.97}Sb_{0.03}$ crystals (which are grown as described by Li *et al.* [3]), several devices with contacts in a Hall bar configuration were fabricated. For all devices in this work, flakes of $Bi_{0.97}Sb_{0.03}$ were exfoliated from single crystals onto SiO_2/Si^{++} substrates. Contact leads were defined using standard e-beam lithography, followed by sputter deposition of 120 nm Nb with a few nm of Pd as capping layer, and lift-off. Then, the flakes themselves were structured using another e-beam lithography step, now followed by Ar^+ milling. Magnetotransport measurements were conducted at 10 K in He-4 cryostats.

The inset of Fig. 2(a) shows a schematic overview of the measurement setup as used for local magnetotransport measurements. A current is sourced through the outer contacts and voltages are measured at the contacts in between. As observed earlier by Kim *et al.* [2], the magnetoresistance of $Bi_{0.97}Sb_{0.03}$, shown in Fig. 2(a), exhibits negative magnetoresistance for parallel electric and magnetic fields. This negative magnetoresistance is considered to be an indication of the CME [2,13–15]. While the CME in $Bi_{0.97}Sb_{0.03}$ originates from the bulk electrons, the magnetoresistance data shows no Shubnikov-de Haas (SdH) oscillations corresponding to the bulk electron pockets, despite the low effective mass and high mobility of these electrons [16]. We will comment on this later. However, in accordance with previous measurements on flakes of $Bi_{0.97}Sb_{0.03}$, we do observe SdH oscillations originating from the bulk hole pocket in different samples made of the same single crystal (see Sec. B of the Supplemental Material [9]).

Figure 2(b) shows the results of a Hall-type measurement. By tensor inversion of the measured longitudinal and Hall resistances, the longitudinal and transverse conductances were obtained. In Fig. 2(c), the conductances are fitted using a multiband model, which takes two surface and two bulk conduction channels into account [3]. For the bulk electrons, we obtain a bulk electron density of $n_B^e = 3.0\times10^{22}$ m^{-3}, where

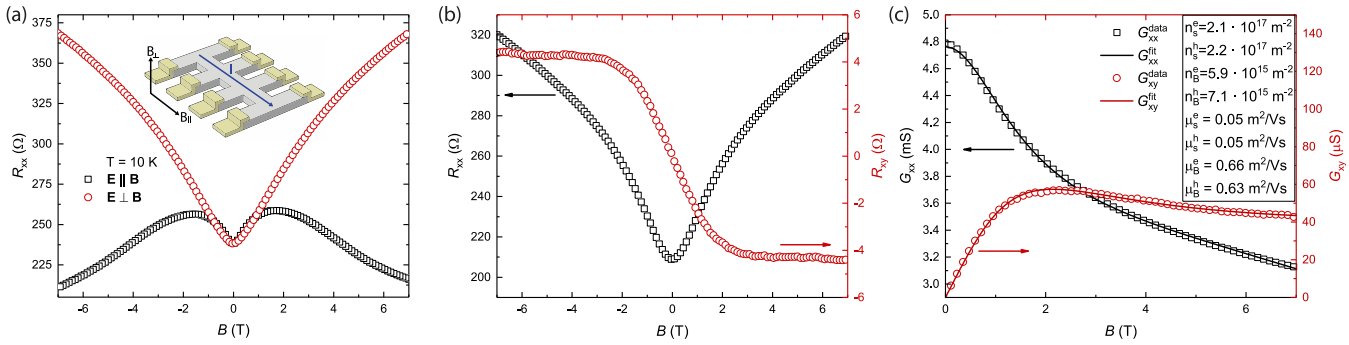

FIG. 2. Local magnetoresistance. (a) Local longitudinal magnetoresistance for perpendicular and parallel electric and magnetic fields. For parallel fields, the MR is strongly negative due to the chiral magnetic effect. Inset: schematic illustration of the device used for local transport. Current is sourced through two of the four outer leads, while the inner four are used as probes for the longitudinal and Hall resistances, as is typical for Hall measurements. (b) Results of the Hall measurement for perpendicular electric and magnetic fields. (c) Drude multiband fit on the conductance. The conductances have been obtained from the measured resistances R_{xx} and R_{xy} through tensor inversion. The low mobility, high carrier density surface state contributions are based on literature [3].

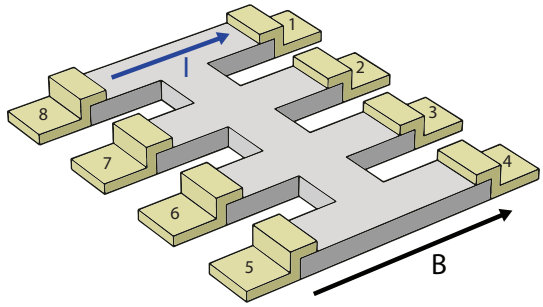

FIG. 3. Nonlocal setup. A schematic illustration of the device used for nonlocal transport measurements (gray represents the $Bi_{0.97}Sb_{0.03}$ flake and yellow the metallic contacts). Current is sourced parallel to the external magnetic field, through two contacts on the side, and the chiral polarization that diffuses into the central channel, is measured at the contacts further along this channel.

we have used a flake thickness of 200 nm. For anisotropic Fermi velocities of $v_1 = 0.8\times10^5$ m/s and $v_2 = 10\times10^5$ m/s [1], this would indicate that the Fermi energy lies only $E_F = \hbar(\pi^2 n_B^e e v_1 v_2/3)^{1/3} = 13$ meV above the Dirac point. The bulk charge carrier mobilities as obtained from the multiband fit are lower than those found in unstructured devices [3]. This is in line with the absence of SdH oscillations in this measurement, which can be attributed to the device dimensions being of the same order as the cyclotron radius, and to disorder due to etching at the device edges. The consequential broadening of the Landau levels does not hamper the presence of the CME [7]. For a conservative effective mass of $m_{e,h} = 0.05\, m_0$ [3], the bulk electron and hole mobilities of $\mu = 0.65$ m^2/Vs give us an estimate of the momentum relaxation time: $\tau_c = \mu m/e \approx 1.8\times10^{-13}$ s. This is in line with the absence of SdH oscillations in this measurement, which can be attributed to the device dimensions being of the same order as the cyclotron radius.

The nonlocal measurement setup is designed such that we can measure the coupling between the polarization of chirality and an external magnetic field at different distances from the polarization source, and is shown in Fig. 3. A current is sourced from contact 8 to 1, as indicated by the blue arrow. By applying a magnetic field parallel to the current, a chiral charge imbalance is induced. As the charge diffuses away from the polarizing source, the polarization becomes weaker and so does the measurable voltage of the polarized charge in the external magnetic field. We measure the voltages locally ($V_L \equiv V_{81} = V_8 - V_1$) and nonlocally ($V_1 \equiv V_{72}$, $V_2 \equiv V_{63}$ and $V_3 \equiv V_{54}$). To be able to distinguish the Ohmic (i.e., normal diffusion) and CME signals, the voltage terminals are located at distances similar to both the expected Ohmic and chiral relaxation lengths.

When studying the CME, in the ideal case one measures the nonlocal response of the chiral anomaly as a function of the applied magnetic field only, i.e., keeping the applied electric field at the source contacts constant. However, due to the low resistance of these samples, we cannot voltage bias our sample and must resort to a current source, thereby causing the current to be constant as a function of the applied magnetic field. When measuring the local electric field, we find that this field is dependent on the magnetic field as well.

In order to obtain a data set with a constant electric field at the source contacts, measurements were performed by sweeping the source current from 0–10 μA for every magnetic field point, resulting in local and nonlocal magnetoresistance curves for a range of source currents $V_{L,1,2,3}(I_s, B)$. An example of such a set of magnetoresistance curves for a fixed source current is shown in Fig. 4(a). The local voltage, $V_L(I_s, B)$, is shown in the inset and should be kept constant, which is achieved by varying the source current $I_s(V_L = \text{cst.}, B)$. In Fig. 4(b), we present the resulting voltages $V_{NL}[I_s(B), B]$, when the local electric field is kept constant in this way. Note that the local voltage, shown in the inset of Fig. 4(b), is now constant. Using this method, the magnetic field dependence of the nonlocal signals can be studied without side effects from the local magnetoresistance. For more information on this procedure, see Sec. C of the Supplemental Material [9].

III. RESULTS

The measured local voltage V_L, presented in the inset of Fig. 4(a), is in good agreement with the expected resistance based on the four-point resistance, taking the size of the channels into account. This indicates that the effects of contact resistances are negligible. Figure 4(b) shows the nonlocal voltages measured at different distances as a function of the applied magnetic field. Here, the electric field at the source

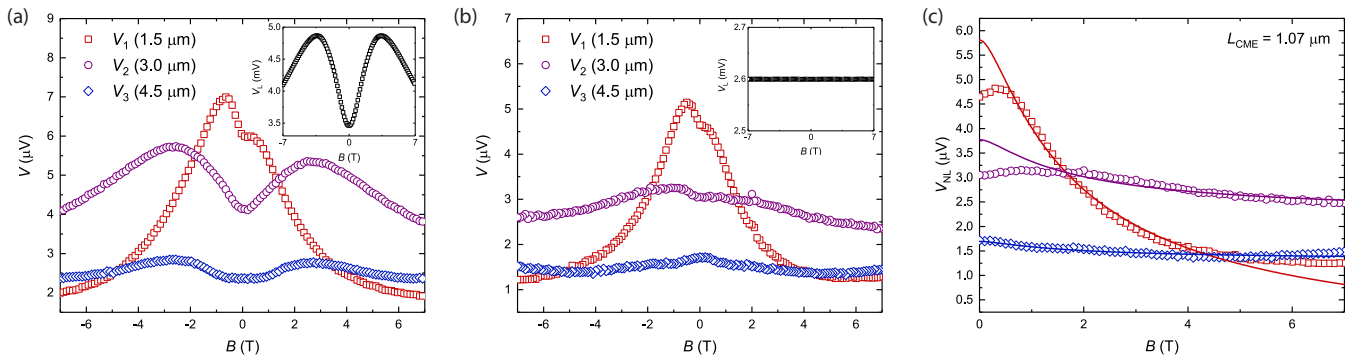

FIG. 4. Nonlocal signals. (a) Measured voltages at distances 1.5, 3 and 4.5 μm. The inset shows the local voltage, measured at the source contacts. (b) Same as in (a), but for a varying source current $I_s(B)$ such that $V_L = \text{cst.}$ (inset). (c) Symmetrized nonlocal voltages for fixed local electric field, $V_{NL}(E = \text{cst.}, B)$, from (b).

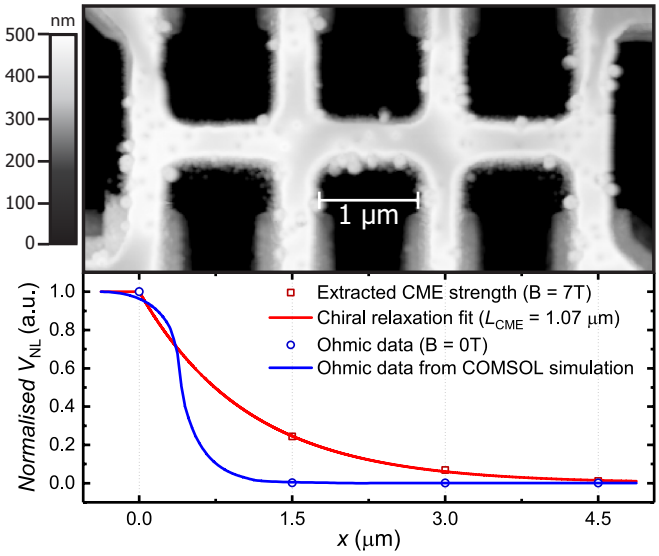

FIG. 5. Diffusion lengths. Top: Atomic force microscopy image of a $Bi_{0.97}Sb_{0.03}$ single-crystal flake, structured into a device for nonlocal measurements and contacted with Nb leads. Bottom: Normalized strength of the Ohmic (zero field) and CME (from fit) contributions to the signals measured at the voltage probes. The CME strength persists over longer distances than the Ohmic signal.

side is kept constant. At zero magnetic field, the measured voltages drop with increasing distance from the source. Furthermore, at all distances we observe a decreasing voltage with increasing magnetic field, which we attribute to the CME. The CME is not dominant for the entire magnetic field range as both at low and high fields, the voltage increases slightly with magnetic field. Kim *et al.* attribute the low field MR to weak antilocalization [2]. High field deviations from the CME signal may originate from higher-order terms, which are not taken into account in this work.

We have identified three possible causes of the small asymmetry of the data. First and foremost is the device asymmetry with respect to the source channel, but variations in sample thickness and imperfections in the structuring process may also be contributing factors. Figure 4(c) shows the symmetrized nonlocal voltages. We fitted the intermediate field data between 2 T and 5.5 T with a model that subtracts the constant Ohmic contribution, and extracts the diffusion of the chiral charge as given by Parameswaran *et al.* [6]:

$$V_{\mathrm{NL}}(x) = -\left(\frac{B}{\gamma + B}\right)^2 e^{-|x|/L_{\mathrm{CME}}} + V_{\mathrm{Ohmic}}. \tag{3}$$

Here x is the distance between the source and the nonlocal probes, γ is proportional to the conductance at the metal contact and L_{CME} is the diffusion length of the chiral charge polarization. The fit agrees well with the data for intermediate magnetic fields and it gives a diffusion length of 1.07 μm. Using $L_{\mathrm{CME}} = \sqrt{D\,\tau_{\mathrm{CME}}}$ and $D = (1/3)\,v_F\,l_m$, with $l_m = v_F\,\tau_{\mathrm{CME}}$, we find a chiral polarization lifetime of $\tau_{\mathrm{CME}} \approx 3.7\times10^{-12}$ s, which is over one order of magnitude longer than the Drude transport lifetime $\tau_c \approx 1.4\times10^{-13}$ s.

The dependence of the normalized Ohmic and CME contributions to the measured voltages is presented in Fig. 5, along with an atomic force microscopy (AFM) image of the device. Here, the amplitudes of the best fits are used to represent the CME strength. The measured Ohmic (zero-field) contribution at all voltage terminals is shown for comparison. The Ohmic contribution of the device is also modeled numerically, where the shown solid curve is a line cut along the horizontal part of the device (see Sec. D of the Supplemental Material [9]). The simulated Ohmic contributions fit very well to the measured data, emphasizing the good homogeneity of the flake. The most notable feature of Fig. 5 is that the chiral polarization of the charge carriers has a significantly longer relaxation length than the Drude transport lifetime.

To study the temperature dependence of the CME in $Bi_{0.97}Sb_{0.03}$, another device was measured at higher temperatures. This device has larger channel widths and spacing as can be seen in the AFM image of the device in Fig. 6(a). Figure 6(b) shows the measured voltages at the nonlocal contacts closest to the source, which present the most striking features. It is apparent that for all temperatures displayed in this figure, the magnetoresistance is strongly negative and that this nonlocal voltage decreases as temperature increases. Through the same fitting procedure described above, the chiral charge polarization diffusion length is extracted for each temperature and shown in Fig. 6(c) (more information on this procedure can be found in Sec. F of the Supplemental Material [9]). In contrast to what has been found for Cd_3As_2

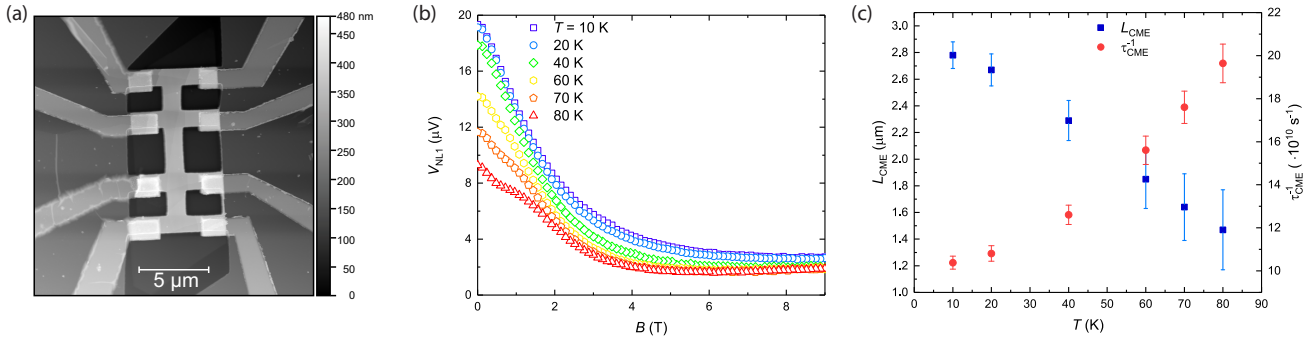

FIG. 6. Temperature dependence of the CME. (a) Atomic force microscopy image of the device used for nonlocal measurements of the CME on a $Bi_{0.97}Sb_{0.03}$ flake at different temperatures. (b) Temperature dependence of the voltage at the nonlocal contact closest to the source. (c) Temperature dependence of the chiral charge diffusion length L_{CME} and the chiral polarization lifetime τ_{CME} as extracted through Eq. (3). For more information, see Sec. F of the Supplemental Material [9].

[7], the chiral diffusion length in $Bi_{0.97}Sb_{0.03}$ does not seem to be constant with increasing temperature, but rather decreases linearly. The increasing relaxation rate τ_{CME}^{-1} with increasing temperature, indicates that inelastic processes are responsible for the relaxation of the chiral polarization in $Bi_{0.97}Sb_{0.03}$.

IV. CONCLUSIONS

In summary, we studied the chiral magnetic effect in $Bi_{0.97}Sb_{0.03}$ through transport measurements in local and nonlocal configurations. First, we characterized the exfoliated crystalline $Bi_{0.97}Sb_{0.03}$ flakes using a Hall-type measurement. Here, we identified contributions from two bulk bands, one of them corresponding to the electron pockets with a linear dispersion and a Fermi level close to the Dirac point. When subjected to parallel electric and magnetic fields, local measurements on our $Bi_{0.97}Sb_{0.03}$ devices show a pronounced negative magnetoresistance, an indication of the chiral magnetic effect.

In a nonlocal configuration, we measured voltages that strongly decrease with increasing magnetic field, which we attribute to the chiral magnetic effect. As voltage contacts are located farther away from the polarization source, the measured chiral magnetic effect weakens. This weakening occurs at a much lower rate than the decay of the Ohmic signal, which is a consequence of the long lifetime of the chiral polarization τ_{CME}. Furthermore, measurements at different temperatures show that the chiral charge diffusion length decreases with increasing temperature, emphasizing the role of inelastic scattering in the chiral charge relaxation process in $Bi_{0.97}Sb_{0.03}$. Both local and nonlocal measurements provide strong evidence of the presence of the chiral magnetic effect in the three-dimensional Dirac semimetal $Bi_{0.97}Sb_{0.03}$.

ACKNOWLEDGMENTS

The authors would like to thank T. Hashimoto for fruitful discussions and acknowledge financial support from the European Research Council (ERC) through a Consolidator Grant and from the Netherlands Organization for Scientific Research (NWO) through a Vici Grant.

[1] D. Hsieh, D. Qian, L. Wray, Y. Xia, Y. S. Hor, R. J. Cava, and M. Z. Hasan, Nature (London) **452**, 970 (2008).
[2] H. J. Kim, K. S. Kim, J. F. Wang, M. Sasaki, N. Satoh, A. Ohnishi, M. Kitaura, M. Yang, and L. Li, Phys. Rev. Lett. **111**, 246603 (2013).
[3] C. Li, J. C. de Boer, B. de Ronde, S. V. Ramankutty, E. van Heumen, Y. Huang, A. de Visser, A. A. Golubov, M. S. Golden, and A. Brinkman, Nat. Mater. **17**, 875 (2018).
[4] B. J. Yang and N. Nagaosa, Nat. Commun. **5**, 4898 (2014).
[5] S. Liang, J. Lin, S. Kushwaha, J. Xing, N. Ni, R. J. Cava, and N. P. Ong, Phys. Rev. X **8**, 031002 (2018).
[6] S. A. Parameswaran, T. Grover, D. A. Abanin, D. A. Pesin, and A. Vishwanath, Phys. Rev. X **4**, 031035 (2014).
[7] C. Zhang, E. Zhang, W. Wang, Y. Liu, Z. G. Chen, S. Lu, S. Liang, J. Cao, X. Yuan, L. Tang, Q. Li, C. Zhou, T. Gu, Y. Wu, J. Zou, and F. Xiu, Nat. Commun. **8**, 13741 (2017).
[8] P. J. W. Moll, N. L. Nair, T. Helm, A. C. Potter, I. Kimchi, A. Vishwanath, and J. G. Analytis, Nature (London) **535**, 266 (2016).
[9] See Supplemental Material at http://link.aps.org/supplemental/10.1103/PhysRevB.99.085124 for the effective Hamiltonian and the chiral magnetic effect, local transport data, a discussion on the constant local electric field, modeling of the Ohmic contribution, nonlocal measurements at perpendicular electric and magnetic fields and the temperature dependence of the chiral diffusion length.
[10] H. B. Nielsen and M. Ninomiya, Phys. Lett. B **130**, 389 (1983).
[11] D. T. Son and B. Z. Spivak, Phys. Rev. B **88**, 104412 (2013).
[12] A. A. Zyuzin and A. A. Burkov, Phys. Rev. B **86**, 115133 (2012).
[13] Q. Li, D. E. Kharzeev, C. Zhang, Y. Huang, I. Pletikosić, A. V. Fedorov, R. D. Zhong, J. A. Schneeloch, G. D. Gu, and T. Valla, Nat. Phys. **12**, 550 (2016).
[14] H. Li, H. He, H. Z. Lu, H. Zhang, H. Liu, R. Ma, Z. Fan, S. Q. Shen, and J. Wang, Nat. Commun. **7**, 10301 (2016).
[15] C. Z. Li, L. X. Wang, H. Liu, J. Wang, Z. M. Liao, and D. P. Yu, Nat. Commun. **6**, 10137 (2015).
[16] Y. Liu and R. E. Allen, Phys. Rev. B **52**, 1566 (1995).